Correlated band structure of NiO, CoO, and MnO by variational cluster approximation

R. Eder
Forschungszentrum Karlsruhe, Institut für Festkörperphysik, 76021 Karlsruhe, Germany
(Received 3 June 2008; revised manuscript received 5 August 2008; published 15 September 2008)

The variational cluster approximation proposed by Potthoff is applied to the calculation of the single-particle spectral function of the transition-metal oxides MnO, CoO, and NiO. Trial self-energies and the numerical value of the Luttinger-Ward functional are obtained by exact diagonalization of a TMO_6 cluster. The single-particle parameters of this cluster serve as variational parameters to construct a stationary point of the grand potential of the lattice system. The stationary point is found by a crossover procedure, which allows to go continuously from an array of disconnected clusters to the lattice system. The self-energy is found to contain irrelevant degrees of freedom, which have marginal impact on the grand potential and need to be excluded to obtain meaningful results. The obtained spectral functions are in good agreement with experimental data.

DOI: 10.1103/PhysRevB.78.115111 PACS number(s): 72.80.Ga, 71.27.+a, 79.60.−i

I. INTRODUCTION

The theoretical description of compounds containing partially filled $3d$, $4f$, or $5f$ shells is a much-studied problem in solid-state theory. Due to the small spatial extent of these shells, the Coulomb repulsion between the electrons in the conduction bands formed from these shells becomes unusually strong and approximations that rely on a mapping of the physical electron system onto one of the fictitious free particles in a suitably constructed effective potential—as is the case in density-functional theory[1] in the local-density approximation (LDA)—cannot even qualitatively describe the resulting state. A frequently cited example is the transition-metal (TM) oxides NiO, CoO, and MnO. Band structure calculations for the paramagnetic phase predict these materials to be metallic while experimentally they remain insulators well above their respective Néel temperature. For NiO and MnO, an insulating ground state can be obtained in the framework of band theory by introducing antiferromagnetic order—for CoO, on the other hand, even the antiferromagnetic ground state is metallic.[2] From a comparison of x-ray photoemission spectroscopy (XPS) and bremsstrahlung isochromat spectroscopy (BIS), it was found[3] that the band gap predicted by LDA for the antiferromagnetic state is too small by a factor of ≈ 10. Moreover electron spectroscopy shows that the electronic structure remains essentially unchanged at the Néel temperature for both NiO (Ref. 4) and CoO.[5] In both compounds there is practically no difference between the electronic spectra in the antiferromagnetic and paramagnetic phases. The same holds true for the related compound NiS where LDA band-structure calculations, on the contrary, predict that the transition to the magnetically ordered phase is accompanied by a significant change of the electronic structure.[6]

Failure to predict the insulating ground state and the magnitude of the insulating gap is not the only shortcoming of LDA. In valence-band photoemission spectroscopy (PES), all three oxides NiO, CoO, and MnO show a "satellite" at an energy of $\approx 6-8$ eV below the valence-band top.[5,7,8] The Fano-like intensity variation with photon energy at the TM $3p \rightarrow 3d$ threshold identifies this feature as being due to $d^n \rightarrow d^{n-1}$ transitions.[9] This part of the electronic structure is not at all reproduced by band-structure calculations, which on the contrary would predict the $d^n \rightarrow d^{n-1}$ transitions near the valence-band top. Finally experimental band structures measured by angle-resolved photoelectron spectroscopy (ARPES) show that for all compounds, i.e., NiO, CoO, and MnO, the TM-derived bands near the valence-band top are almost dispersionless.[5,8,10] This is also in contradiction to LDA calculations, which predicts band widths of around 2 eV for the TM $3d$-derived bands.

Starting with the work of Hubbard,[11] a variety of theoretical methods have been invented to deal with this problem.[12–22] Major progress toward a quantitative description of $3d$TM oxides has been made by the cluster method initiated by Fujimori and co-workers,[23,24] and van Elp and co-workers.[25–27] This takes the opposite point of view as compared to band theory, namely to abandon translational invariance and instead treat exactly—by means of atomic multiplet theory[28,29]—the Coulomb interaction in the $3d$ shell of a TM ion in an octahedral "cage" of nearest-neighbor oxygen atoms. The angle-integrated valence-band photoemission spectra calculated by this method are in excellent agreement with experiment.[23–27] This is clear evidence that the atomic multiplets of the partly filled $3d$ shell—suitably modified by the crystalline electric field (CEF)—persist in the solid and play an important part in the physics. On the other hand due to its "impurity" character, the cluster method can only give $\mathbf{k}$-independent quantities.

Recently, however, ideas have been put forward to broaden the correlated ionization and affinity states of finite clusters into bands.[30–32] A particularly elegant way to do so—the variational cluster approximation (VCA)—has been proposed by Potthoff.[33] Building on field-theoretical work of Luttinger and Ward,[34] who showed that the grand canonical potential Ω of an interacting Fermion system is stationary with respect to variations of the electronic self-energy $\Sigma(\omega)$, Potthoff proposed to generate trial self-energies numerically by exact diagonalization of finite clusters and use them in a variational scheme for Ω. This amounts to finding the best approximation to the true self-energy of the lattice among the subset of "cluster representable" ones, i.e., exact self-energies of finite clusters.

So far the VCA has been applied mainly to simplified systems such as the single-band Hubbard model.[33,35] How-

ever, the success of the cluster method for TM oxides clearly suggests applying the VCA also to a realistic model for TM oxides, thereby using the octahedral clusters introduced by Fujimori and Minami to generate self-energies. Here we outline such a calculation for NiO, CoO, and MnO, in which all have the rocksalt structure. For simplicity we neglect any of the lattice distortions observed in the actual compounds as well as the antiferromagnetic order at low temperature, and study the ideal rocksalt structure in the paramagnetic phase. As already mentioned, the single-particle spectra of these compounds do not change appreciably during the Néel transition so this is probably a reasonable assumption. A preliminary study for NiO using the VCA has been published elsewhere.[36]

Using clusters containing just a single TM ion implies that the self-energy is site diagonal, i.e., **k** independent. The corresponding approximation thus is similar to the dynamical mean-field theory (DMFT) calculations, which have recently been applied to a variety of compounds.[37] The relationship between DMFT and the VCA has been discussed in detail by Potthoff,[33] and a detailed comparison with recent DMFT calculations for NiO will be presented below.

II. HAMILTONIAN

We start by defining the Hamiltonian, which describes the correlated transition-metal oxide (TMO) lattice. We use a linear combination of atomic orbitals (LCAO) parametrization of the noninteracting part H_0. Denoting by $d^\dagger_{i,\alpha,\sigma}$ an operator that creates a spin-σ electron in the TM3d-orbital $\alpha \in \{xy, xz, yz, \ldots\}$ on site i and by $p_{j,\lambda,\sigma}$ annihilates a spin-σ electron in O 2p orbital $\lambda \in \{x, y, z\}$ on site j, the single-particle terms read

$$H_0 = \sum_{i,\alpha,j,\lambda} \sum_{\sigma} (t^{j,\lambda}_{i,\alpha} d^\dagger_{i,\alpha,\sigma} p_{j,\lambda,\sigma} + \text{H.c.}) + \sum_{i,\alpha,\sigma} \epsilon_\alpha d^\dagger_{i,\alpha,\sigma} d_{i,\alpha,\sigma} + \sum_{j,\lambda,\sigma} \epsilon_p p^\dagger_{j,\lambda,\sigma} p_{j,\lambda,\sigma}. \quad (1)$$

Here $\epsilon_\alpha = \epsilon_d + 6Dq$ for e_g orbitals and $\epsilon_\alpha = \epsilon_d - 4Dq$ for t_{2g}. The transfer integrals $t^{j,\lambda}_{i,\alpha}$ can be expressed in terms of LCAO parameters (two-center integrals) and the difference $\mathbf{R_i} - \mathbf{R_j}$ by using the Slater-Koster tables.[38] The Hamiltonian also contains analogous terms that describe hybridization between next-nearest neighbors, i.e., O 2p-O 2p and Ni 3d-Ni 3d. The LCAO parameters and site energies ϵ have been obtained from a fit to an LDA band structure, thereby closely following the procedure outlined by Mattheiss.[39] The parameters so obtained are listed in Table I. To give an impression about what accuracy can be expected from such a fit, Fig. 1 shows the actual LDA band structure and the LCAO fit for CoO. Following Mattheiss[39] an O 2s orbital was included into the basis set in addition to the O 2p and TM3d orbitals. This turned out to be crucial for a correct fit of the dispersion of some TM3d-like bands along $\Gamma - X$. The energy of the O 2s orbital, ϵ_s, has no particular impact on the dispersion of the bands near the Fermi level and for simplicity was kept at 14 eV below the O 2p energy. However, the corresponding LCAO parameter ($sd\sigma$) was determined by the fitting procedure. The fit can be improved substantially by including also nonvanishing overlap integrals between O 2p and TM3d orbitals; since, however, the VCA needs well-defined TM3d orbitals to which the self-energy can be added, these overlap integrals were omitted. The hybridization element ($dd\delta$) turned out to be meaningful only in combination with these overlap integrals—a fit without overlap produced a positive value of ($dd\delta$)—and hence was set to be zero. By and large the variation of the hybridization integrals

TABLE I. Hybridization integrals and site energies ϵ (in electron volts) obtained by a LCAO fit to paramagnetic LDA band structures. The site energies have been shifted so as to have $\epsilon_p = 0$.

	NiO	CoO	MnO
($pp\sigma$)	0.695	0.627	0.542
($pp\pi$)	−0.118	−0.111	−0.108
($sd\sigma$)	−1.210	−1.210	−1.319
($pd\sigma$)	−1.289	−1.276	−1.275
($pd\pi$)	0.614	0.596	0.587
($dd\sigma$)	−0.255	−0.274	−0.331
($dd\pi$)	0.060	0.067	0.097
ϵ_s	−14.000	−14.000	−14.000
ϵ_p	0.000	0.000	0.000
ϵ_d	2.822	3.400	3.899
$10Dq$	0.138	0.142	0.069

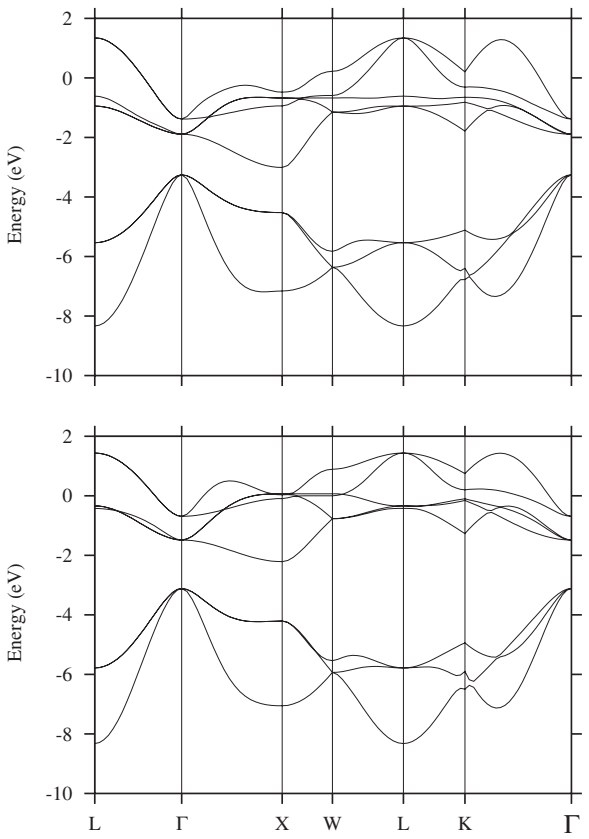

FIG. 1. LDA band structure (top) and LCAO fit (bottom) for CoO.

TABLE II. Energies of the Hund rule ground state $E(d^n)$, and the resulting values of $U=E(d^{n+1})+E(d^{n-1})-2E(d^n)$ and $\Delta=E(d^{n+1}\underline{L})-E(d^n)$, expressed in terms of the Racah parameters and $\Delta^*=\epsilon_d^*-\epsilon_p$.

n	$E(d^n)$	U	Δ
9	$36A-56B+28C$		
8	$28A-50B+21C$	$A+B$	$\Delta^*+8A-6B+7C$
7	$18A-28B+14C$	$A+B$	$\Delta^*+7A-7B+14C$
6	$15A-35B+7C$	$A-8B$	$\Delta^*+6A-8B+7C$
5	$10A-35B$	$A+14B+7C$	$\Delta^*+5A+7C$
4	$6A-21B$		

along the series NiO→MnO is consistent with the increasing lattice constant on one hand and the increasing d-shell radius on the other. The parameters moreover are similar to previous estimates in the literature.[23,25]

We proceed to the interaction terms of the Hamiltonian. The Coulomb interaction within the d shell can be written as

$$H_1=\sum_{\kappa_1,\kappa_2,\kappa_3,\kappa_4}(\kappa_1\kappa_2|g|\kappa_4\kappa_3)d^\dagger_{\kappa_1}d^\dagger_{\kappa_2}d_{\kappa_3}d_{\kappa_4}. \quad (2)$$

Here we have suppressed the site label i and $\kappa=(m,\sigma)$, where $m\in\{-2,-1,\ldots 2\}$ denotes the z component of orbital angular momentum. The Coulomb matrix elements $(\kappa_1\kappa_2|g|\kappa_4\kappa_3)$ can be expressed[28,29,40] in terms of the three Racah parameters, A, B, and C. Due to the "breathing" of the $3d$ radial-wave function, these parameters should be taken depending on the d-shell occupation.[23] This, however, would create an "implicit" interaction containing terms higher than quartic in the Fermion operators, and also an interaction between d and p electrons. This would defeat our formalism and we therefore do not take the dependence on d-shell occupation into account. The parameters B and C can be estimated from atomic Hartree-Fock wave functions, and here we use the values given in Refs. 25–27 for the three materials under study. The parameter A is reduced substantially from its atomic value by solid-state screening. This parameter can in principle be obtained from density-functional calculations.[41,42] In the cluster calculations for TM oxides,[23–27] A is usually treated as an adjustable parameter and here we do the same. Adjusting A is equivalent to adjusting the "Hubbard U"$=E(d^{n+1})+E(d^{n-1})-2E(d^n)$, where $E(d^n)$ denotes the energy of a d shell with n electrons. There is some ambiguity as to what exactly is to be understood by "the energy of d^n"; here we follow Refs. 25–27 and take $E(d^n)$ to be the Coulomb energy of the Hund rule ground state of the free ion i.e., calculated without CEF splitting. $E(d^n)$—and hence U—can be expressed in terms of the Racah parameters,[29] and these expressions are listed in Table II. Another way to define a Hubbard U would be to note that the average Coulomb energy of the d^n multiplets is[28,29]

$$E=\frac{n(n-1)}{2}\left(A-\frac{14}{9}B+\frac{7}{9}C\right), \quad (3)$$

which would suggest defining $U_{av}=A-\frac{14}{9}B+\frac{7}{9}$C. This average Coulomb repulsion, which does not include exchange effects, may be compared to the values U_{CDF} obtained by constrained density-functional calculations.[41]

TABLE III. Racah parameters, bare d-level energy ϵ_d^*, Hubbard U, and charge-transfer energy Δ (according to Table II) for the three materials studied. Also given are the average Hubbard U U_{av} according to Eq. (3), the Coulomb parameter U_{CDF} from constrained density-functional calculation (Ref. 41), the electron number per d orbital n_d as obtained from the LDA calculation, and the estimate for the d-level energy $\tilde{\epsilon}_d^*$ according to Eq. (4). All energies are in electron volts.

	NiO	CoO	MnO
A	8.25	7.2	6.1
B	0.13	0.14	0.12
C	0.60	0.54	0.41
ϵ_d^*	−62.0	−45.5	−23.3
U	8.38	7.34	10.65
Δ	7.42	11.48	10.07
U_{av}	8.51	7.40	6.23
U_{CDF}	8.00	7.80	6.90
n_d	0.85	0.76	0.56
$\tilde{\epsilon}_d^*$	−60.53	−45.81	−26.91

A second parameter, which is of importance for charge-transfer systems[43] that is usually adjusted to experiment, is the "bare" d-level energy ϵ_d^* or equivalently the charge-transfer energy $\Delta=E(d^{n+1}\underline{L})-E(d^n)$. Expressing the $E(d^n)$ in terms of Racah parameters, Δ can be expressed in terms of these and the difference $\Delta^*=\epsilon_d^*-\epsilon_p$ (see Table II). The values of ϵ_d^* used in the present calculation are given in Table III as well. It should be noted that, while the LCAO fit actually gives an energy for the site energies ϵ_d (see Table I), these values already incorporate the Coulomb interaction between d electrons. Since in our formalism the Coulomb interaction is described by the Hamiltonian [Eq. (2)], one would have to subtract it off to avoid double counting. Namely if one considers the Hubbard U as known, one may estimate the bare value $\tilde{\epsilon}_d^*$ from the LDA site energy ϵ_d and the d-level occupancies n_d as[20]

$$\tilde{\epsilon}_d^*=\epsilon_d-9U_{av}n_d. \quad (4)$$

The estimates obtained in this way are also listed in Table III. For NiO and CoO these corrected LDA values are close to the adjusted parameters ϵ_d^* used in the actual calculation. The situation is different for MnO but for this compound the U obtained from ground-state energies also differs strongly from the multiplet average U_{av}. The reason for this is the strong exchange stabilization in the high-spin ground state of d^5 (see Table II) and one may not hope to obtain agreement between the two estimates for the site energy either. The reason is simply that a Hubbard U is not uniquely defined in the presence of strong multiplet splitting. Finally, any Coulomb interaction between electrons that are not in the same TM3d shell is neglected.

To summarize, the lattice Hamiltonian comprises two terms: first, the single-particle terms [Eq. (1)] with the pa-

rameters in Table I but with ϵ_d replaced by ϵ_d^* given in Table III to avoid double counting of the Coulomb interaction in the d shell. Second the interaction term [Eq. (2)] with the Racah parameters A, B, and C in Table III. Let us stress that the parameters A and ϵ_d^* have been adjusted such that the insulating gap and binding energy of the satellite come out as in experiment—as can be seen from Table III. However, these adjusted values are reasonably consistent with estimates from density-functional calculations. Finally, the value of the chemical potential was $\mu=5.5$ eV for NiO and CoO, and $\mu=7$ eV for MnO.

III. VARIATIONAL CLUSTER APPROXIMATION

Having specified the strongly correlated problem under discussion, we outline the variational cluster approximation. This is based on an expression for the grand potential Ω of an interacting many-Fermion system derived by Luttinger and Ward.[34] In a multiband system where the Green function $\mathbf{G}(\mathbf{k},\omega)$, the noninteracting kinetic energy $\mathbf{t}(\mathbf{k})$, and the self-energy $\mathbf{\Sigma}(\mathbf{k},\omega)$ for given energy ω and momentum $\mathbf{k}$ are matrices of dimension $2n\times 2n$, with n as the number of orbitals in the unit cell, it reads[44]

$$\Omega = -\frac{1}{\beta}\sum_{\mathbf{k},\nu} e^{\omega_\nu 0^+} \ln \det[-\mathbf{G}^{-1}(\mathbf{k},\omega_\nu) + F(\mathbf{\Sigma})], \tag{5}$$

where $\omega_\nu=(2\nu+1)\pi/\beta$, with β as the inverse temperature, are the Fermionic Matsubara frequencies,

$$\mathbf{G}^{-1}(\mathbf{k},\omega) = \omega + \mu - \mathbf{t}(\mathbf{k}) - \mathbf{\Sigma}(\mathbf{k},\omega), \tag{6}$$

with μ as the chemical potential and the functional $F[\mathbf{\Sigma}]$ is the Legendre transform of the Luttinger-Ward functional $\Phi[\mathbf{G}]$. The latter is defined[34] as the sum of all closed linked skeleton diagrams with the noninteracting Green functions replaced by the full Green functions. A nonperturbative derivation of a functional with the same properties as Φ has recently been given by Potthoff.[45] $\Phi[\mathbf{G}]$ is the generating functional of the self-energy $\mathbf{\Sigma}$, i.e.,

$$\frac{1}{\beta}\Sigma_{ij}(\mathbf{k},\omega_\nu) = \frac{\partial \Phi}{\partial G_{ji}(\mathbf{k},\omega_\nu)}, \tag{7}$$

and $F[\mathbf{\Sigma}]$ is obtained by Legendre transform to eliminate $\mathbf{G}$ in favor of $\mathbf{\Sigma}$:

$$F[\mathbf{\Sigma}] = \Phi[\mathbf{G}] - \frac{1}{\beta}\sum_{\mathbf{k},\nu} \mathrm{trace}\{[\mathbf{G}(\mathbf{k},\omega_\nu)\mathbf{\Sigma}(\mathbf{k},\omega_\nu)]\ .$$

By virtue of being a Legendre transform, it obeys

$$\frac{1}{\beta}G_{ij}(\mathbf{k},\omega_\nu) = -\frac{\partial F}{\partial \Sigma_{ji}(\mathbf{k},\omega_\nu)}, \tag{8}$$

and using the identity

$$\frac{\partial}{\partial A_{ij}} \ln \det A = (A^{-1})_{ji}, \tag{9}$$

which holds for any matrix A with $\det A \neq 0$ as well as the Dyson Eq. (6), we find that Ω is stationary with respect to variations of Σ:

$$\frac{\partial \Omega}{\partial \Sigma_{ij}(\mathbf{k},\omega_\nu)} = 0. \tag{10}$$

The crucial obstacle in exploiting this stationarity property in a variational scheme for the self-energy $\mathbf{\Sigma}$ is the evaluation of the functional $F[\mathbf{\Sigma}]$ for a given "trial $\mathbf{\Sigma}$". Potthoff's solution[33] makes use of the fact that, just like $\Phi[\mathbf{G}]$, $F[\mathbf{\Sigma}]$ has no explicit dependence on the single-particle terms of H and therefore is the same functional of $\mathbf{\Sigma}$ for any two systems with the same interaction part of the Hamiltonian. This is easily seen from the diagrammatic representation of $\Phi[\mathbf{G}]$ because the expression associated with a given Feynman diagram involves only the interaction matrix elements and the Green function itself.

In the VCA this independence of $F[\mathbf{\Sigma}]$ on the single-particle terms of the Hamiltonian is used to construct trial self-energies by exact diagonalization of finite clusters and thereby obtain the exact numerical value of $F[\mathbf{\Sigma}]$. In a first step one chooses a so-called reference system, which has the same interaction part as the lattice problem under study but consists of disconnected finite clusters. If the interaction terms are short ranged, which is the reason for keeping only the Coulomb interaction between electrons in the same d shell, this can always be achieved by suitable choice of the single-particle terms. The disconnected finite clusters of the reference system then are solved by exact diagonalization, which gives the eigenenergies ϵ_ν and wave functions $|\Phi_\nu\rangle$ for all particle numbers in the cluster. Of course this sets some limit on the size of the clusters. Next, the Green function $\widetilde{\mathbf{G}}(\omega)$ and grand potential $\widetilde{\Omega}$ of the reference system are calculated numerically, and Eq. (5) is reverted to express the exact numerical value of $F[\mathbf{\Sigma}]$ in terms of these. This simply means that the summation of infinitely many Feynman diagrams and Legendre transform is done implicitly in the course of the exact diagonalization of the reference system. Then, the self-energy $\mathbf{\Sigma}(\omega)$ of the reference system, which is readily extracted from the Dyson equation for $\widetilde{\mathbf{G}}(\omega)$, can be used as a trial self-energy for the lattice system. Therefore the numerical value of $F[\mathbf{\Sigma}]$ calculated in the cluster is simply inserted into the Luttinger-Ward formula (5) for the grand potential of the physical (i.e., lattice) system. The variation of $\mathbf{\Sigma}(\omega)$ is performed by varying the single-electron parameters—such as hybridization integrals or site energies—of the reference system.

In applying this procedure one frequently has to evaluate expressions of the type (the momentum $\boldsymbol{k}$ is suppressed for brevity),

$$S = -\frac{1}{\beta}\sum_{\nu} e^{\omega_\nu 0^+} \ln \det[-\boldsymbol{G}^{-1}(\omega_\nu)]. \tag{11}$$

To evaluate this we closely follow Luttinger and Ward,[34] and first convert the sum into a contour integral,

$$-\frac{1}{\beta}\sum_{\nu} g(\omega_\nu) \to \frac{1}{2\pi i}\int_{C_0} f(\omega)g(\omega)d\omega, \tag{12}$$

where $f(\omega)$ is the Fermi function and C_0 is the standard contour encircling the singularities of the Fermi function in

counterclockwise direction. Next we deform the contour so that it encircles the singularities of the logarithm, which are all located on the real axis (see the Appendix). Following Luttinger and Ward we then use

$$f(\omega) = -\frac{1}{\beta}\frac{d}{d\omega}\log(1+e^{-\beta\omega}), \tag{13}$$

and integrate by parts. Using Eq. (9) we thus obtain

$$S = \frac{1}{2\pi\beta i}\int_C d\omega \log(1+e^{-\beta\omega})\mathrm{trace}\left\{\left[1-\frac{d\Sigma(\omega)}{d\omega}\right]\boldsymbol{G}(\omega)\right\}, \tag{14}$$

where C is a contour that encircles the singularities of trace in clockwise fashion. This can now be evaluated by numerical contour integration. To derive the expression given by Potthoff, we note the alternative expression

$$S = \frac{-1}{2\pi\beta i}\int_C d\omega \log(1+e^{-\beta\omega})\sum_i \frac{1}{\lambda_i(\omega)}\frac{\partial\lambda_i(\omega)}{\partial\omega},$$

where $\lambda_i(\omega)$ are the eigenvalues of $\boldsymbol{G}(\omega)$. There are two types of singularities of this expression: (a) zeros of an eigenvalue, i.e.,

$$\lambda(\omega) \approx a_\nu(\omega-\zeta_\nu) \rightarrow \frac{1}{\lambda(\omega)}\frac{\partial\lambda(\omega)}{\partial\omega} = \frac{1}{\omega-\zeta_\nu},$$

and (b) singularities of an eigenvalue, i.e.,

$$\lambda(\omega) \approx \frac{b_\mu}{\omega-\eta_\mu} \rightarrow \frac{1}{\lambda(\omega)}\frac{\partial\lambda(\omega)}{\partial\omega} = -\frac{1}{\omega-\eta_\mu}.$$

Hence

$$S = -\frac{1}{\beta}\left[\sum_\mu \log(1+e^{-\beta\eta_\mu}) - \sum_\nu \log(1+e^{-\beta\zeta_\nu})\right],$$

i.e., the expression derived by Potthoff.[33]

For the numerical evaluation of S, a slightly different procedure is more convenient. For Matsubara frequencies ω_ν with $|\nu| \le \nu_{\max}$, the respective terms in the sum [Eq. (11)] are evaluated directly by computing the eigenvalues of $\boldsymbol{G}^{-1}(\omega)$. For $|\nu| > \nu_{\max}$ we switch to a contour integral using Eq. (12) and deform the integration contour, as indicated in Fig. 2. Along C_1 and C_4 the integral is evaluated numerically again by calculating the eigenvalues of $\boldsymbol{G}^{-1}(\omega)$. Along the positive real axis, the integrand thereby is cut off by the Fermi function. Along C_2 and C_3 we integrate by parts using again Eq. (13) and deform the two pieces into the short piece C_5, which is possible because the contour encloses no more singularities of the integrand. It is not possible to integrate by parts along C_1 and C_4 because these contours cross the lines—indicated by dashed lines in Fig. 2—where $\log(1+e^{-\beta\omega})$ has branch cuts. The advantage of this procedure is that the resulting integration contour $C_1-C_5-C_4$ can be kept far from the singularities of the Green function and self-energy on the real axis so that the integrand will always be a smooth function, and a numerical integration with relatively few mesh points (of order 10^3) gives accurate results.

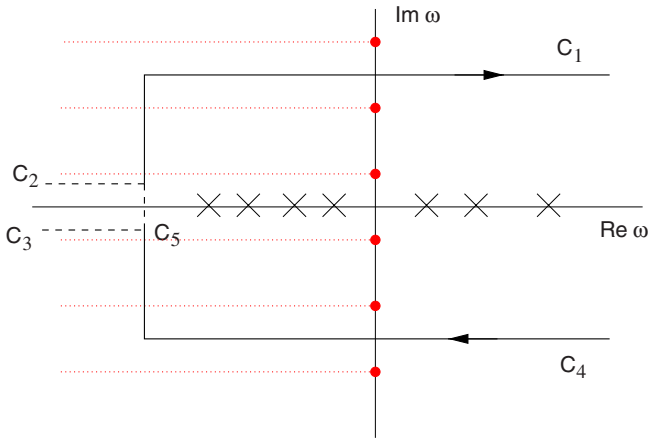

FIG. 2. (Color online) Integration contour for the numerical evaluation of S. The dots on the imaginary axis denote the Matsubara frequencies and the dotted lines are branch cuts of $\log(1+e^{-\beta\omega})$. Crosses denote poles of the Green function.

IV. REFERENCE SYSTEM

Given the excellent results obtained by the cluster method for angle-integrated spectra,[23–27] it seems natural to use clusters that are equivalent to TMO_6 octahedra as reference system. More precisely we choose a reference system where each TM3d orbital d_α is coupled to one "ligand" orbital L_α, with these ligands in turn decoupled from each other, and the interaction within the d shell given by Eq. (2). The reference system thus is equivalent to an array of nonoverlapping identical TMO_6 clusters where each ligand L_α corresponds to the unique linear combination of O 2p orbitals on the six nearest O neighbors of a given TM atom, which hybridizes with the TM3d_α orbital (see Fig. 3). We write the single-particle Hamiltonian for a TML_5 cluster as

$$H_{\mathrm{single}} = \sum_{\alpha,\sigma} V(\alpha)(d^\dagger_{\alpha,\sigma}L_{\alpha,\sigma} + \mathrm{H.c.}) + \sum_{\alpha,\sigma}[E(\alpha)d^\dagger_{\alpha,\sigma}d_{\alpha,\sigma} + e(\alpha)L^\dagger_{\alpha,\sigma}L_{\alpha,\sigma}]. \tag{15}$$

The variational parameters thus are the hopping matrix ele-

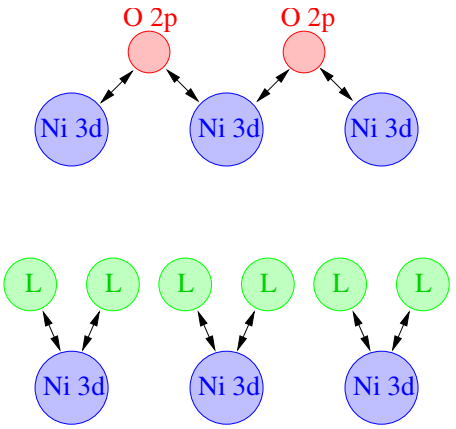

FIG. 3. (Color online) Physical (top) and reference (bottom) systems. Arrows indicate nonvanishing hybridization. While the physical system is a true lattice, the reference system is an array of disconnected clusters. The Coulomb interaction between electrons in the TM d shell is the same for both systems.

ments (V_α), the ligand energies $e(\alpha)$, and the d-level energies $E(\alpha)$ with $\alpha \in \{e_g, t_{2g}\}$; in total we thus have six parameters. It is convenient to rewrite the site energies in the reference system as follows:

$$E(e_g) = \epsilon_0 - \epsilon_1 + 3\epsilon_2/5 + \epsilon_d^*, \tag{16}$$

$$E(t_{2g}) = \epsilon_0 - \epsilon_1 - 2\epsilon_2/5 + \epsilon_d^*, \tag{17}$$

$$e(e_g) = \epsilon_0 + \epsilon_1 + 3\epsilon_3/5, \tag{18}$$

and

$$e(t_{2g}) = \epsilon_0 + \epsilon_1 - 2\epsilon_3/5. \tag{19}$$

As shown by Aichhorn *et al.*[35] optimization of the "center of gravity" ϵ_0 ensures that the electron number obtained by differentiating Ω with respect to μ is equal to the result obtained by integrating the spectral function. It should be stressed here that the VCA necessitates that the chemical potential μ be identical between lattice and reference systems.

To compute the Green function for the reference system, all eigenstates $|\nu\rangle$ with an expectation value $\langle\nu|H-\mu N|\nu\rangle$, which is less than 50 k_BT above the minimum value, are obtained by the Lanczos method. Excited states can be computed by replacing

$$H \to H + E\sum_{\lambda=1}^{\nu-1} |\lambda\rangle\langle\lambda|$$

in the Lanczos iteration for the νth eigenstate where E is a large positive constant. This allows computation of up to 20 low lying states without problems, which turns out to be quite sufficient for the temperatures studied. The correctness of the wave functions is checked by computing the expectation value of the square of the spin $\langle\nu|\vec{S}^2|\nu\rangle$ for each eigenstate and checking that it agrees with an allowed value to computer accuracy. Also the expectation values of the operators for C_2 and C_4 are computed and summed for all states of one degenerate level, and it is checked that the sums agree with the known characters of one of the irreducible representations of the cubic group to computer accuracy. In this way one can be rather certain that no state is missed and that the wave functions are accurate. The Green function then is calculated for each $|\nu\rangle$ by the Lanczos method and the resulting functions are added with their proper thermal weights. Off-diagonal elements of the Green function are obtained by a subtraction procedure.[46] It follows from symmetry that the 10×10 Green function is block diagonal and consists of five 2×2 subblocks, whereby the two e_g-like blocks and the three t_{2g}-like blocks are equal. These are inverted and the self-energy is obtained by the Dyson equation. A good check for the accuracy of the calculation is provided by the fact that only the (d,d) entry of each 2×2 self-energy matrix may differ from zero. At this point the large distance of the integration curve from the singularities of $\boldsymbol{G}(\omega)$ (see Fig. 2) turns out to be beneficial and makes sure that the nonallowed matrix elements of $\boldsymbol{\Sigma}(\omega)$ are indeed zero to computer accuracy.

The search for the stationary point of a function of six variables λ_i is a difficult task—even more so because the stationary point is not a global minimum or maximum and is in fact not even a local extremum but a saddle point (see below). This problem has motivated the search for functionals other than $\Omega[\Sigma]$, which take an extremum value at the physical self-energy.[47] We can solve this problem in the following way. However, if we have a set of parameters that is sufficiently close to the stationary point, we can evaluate the derivatives $\partial\Omega/\partial\lambda_i$ and $\partial^2\Omega/\partial\lambda_i\partial\lambda_j$ numerically, and use the Newton method to find the point where $\partial\Omega/\partial\lambda_i=0$. Next, instead of the true lattice system, we choose our "physical system" to be a "hybrid system", which contains both the O $2p$-lattice and the ligands for each TM ion (see Fig. 4). We take the TM-O and TM-TM hybridizations to be multiplied by α_1, and the TM-L hybridization by α_2. For $\alpha_1=0$ and $\alpha_2=1$, we therefore have the reference system itself plus a decoupled O $2p$ lattice. For this system the exact stationary point is known—namely the parameters of the reference system itself. On the other hand, for $\alpha_1=1$ and $\alpha_2=0$, we have the physical lattice system plus the decoupled and hence irrelevant ligands, and a solution to this system is a solution to the lattice system itself. That noninteracting and decoupled orbitals do not influence the stationarity properties of the remainder of the system follows first from the fact that noninteracting orbitals do not contribute to $F[\Sigma]$, and second from the property—shown by Luttinger and Ward[34]—that S is equal to Ω for free electrons. Decoupled noninteracting orbitals thus give an identical constant shift to both S and Ω that is independent of the remaining system provided the parameter sets are independent—which is in fact the case.

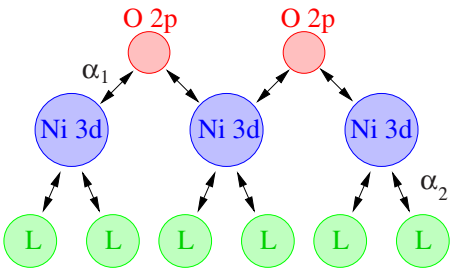

FIG. 4. (Color online) Hybrid system used to find the stationary point of Ω.

In this way we can go continuously from an exactly solvable system to the physical lattice system. In practice we vary the parameters α_1, α_2 in steps of 0.1 and start the Newton method using the stationary values of the preceding step as initial values. When combined with a simple extrapolation procedure, this yields the stationary point of the lattice in $\approx$10 steps with $\leq$2 Newton iterations in each step. Obviously such a crossover procedure can be formulated for other applications of the VCA as well.

We next discuss a second important technical point. Having found the stationary point, we can calculate the matrix of second derivatives $\partial^2\Omega/\partial\lambda_i\partial\lambda_j$ and diagonalize it. Figure 5 shows a scan of Ω through the stationary point of CoO along the principal axes so obtained. There are two important things to recognize. First, the stationary point is a saddle point but the above crossover procedure had no problems finding it. Second there are certain directions in parameter space where Ω shows only an extremely weak variation.

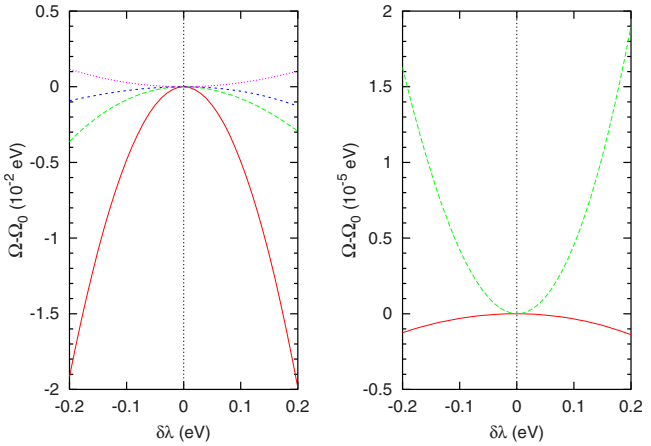

FIG. 5. (Color online) Scans through the stationary point of CoO. The normalized eigenvectors $\mathbf{v}_i$ of $\partial^2\Omega/\partial\lambda_i\partial\lambda_j$ were multiplied by λ_i.

This turned out to be true in all other cases studied as well. This weak variation may either stem from a near invariance of the self-energy under changes of the cluster parameters or the change of the self-energy is appreciable but irrelevant in that it does not change the lattice Ω. The presence of such "nearly invariant lines" in parameter space clearly is undesirable in that it may induce numerical instabilities. It may happen that small changes of Ω due to, e.g., a slightly wrong LCAO band structure or even numerical inaccuracies may drive the stationary point along these lines in parameter space to compensate for them. To simplify matters the number of parameters therefore was reduced. Inspection of the eigenvectors associated with the nearly invariant lines showed that these were predominantly combinations of the parameters ϵ_1 and ϵ_3 in Eq. (19). These parameters have almost no influence on Ω and hence were not subject to variation. The parameter ϵ_1 was set as equal to zero. In the cluster calculation the value for ϵ_3 would be $2(pp\sigma)-2(pp\pi)$ (Ref. 25); for simplicity the value $\epsilon_3=1.4$ eV was used for all three compounds.

Including ϵ_1 and ϵ_3 into the set of parameters to be optimized actually turned out to give unsatisfactory results for the single-particle spectrum. ϵ_1 tended to take on large positive values whereas ϵ_3 usually took large *negative* values. As a net effect this produced spurious photoemission peaks with very small spectral weight that were split off by one or two electron volts from the remainder of the photoemission spectrum, resulting in too small gaps and poor agreement with experiment. Clearly this is a feature of the variational cluster approximation that needs to be clarified. It should be noted that reducing the number of parameters that are optimized simply amounts to restricting the space of trial self-energies. Since optimization of these parameters hardly changes Ω, this is similar to restricting the degrees of freedom in a trial wave function to the most relevant ones. It then seems that an "overoptimization" of parameters leads to poor results. On the other hand the inclusion of irrelevant degrees of freedom into a variational wave function may also be detrimental for properties of the wave function other than the ground-state energy.

TABLE IV. Parameters in the Hamiltonian of the reference system [Eqs. (15)–(18)] for which Ω is stationary at $T=150$ K (in electron volts). Parameters marked by * have not been subjected to variation (see discussion in Sec. IV).

	NiO	CoO	MnO
ϵ_0	0.373	0.031	0.014
ϵ_1	−0.070*	−0.070*	−0.070*
ϵ_2	−0.301	0.266	0.225
ϵ_3	1.400*	1.400*	1.400*
$V(e_g)$	−2.226	−2.261	−2.302
$V(t_{2g})$	1.229*	1.122	1.114

Finally, NiO turned out to be a special case. Since the ground state of d^8 in cubic symmetry is $t_{2g}^6 e_g^2$, the hopping integral $V(t_{2g})$ has practically no impact on Ω because it connects filled orbitals. In fact, derivatives of Ω with respect to $V(t_{2g})$ turned out to be of order 10^{-10}, i.e., well beyond the numerical accuracy of the whole procedure. $V(t_{2g})$ was therefore kept at $2(pd\pi)$, which again is the value expected in the cluster calculation. In a previous VCA study of NiO,[36] a different approach was chosen. There the hopping integral $V(t_{2g})$ was set as equal to zero. This implies that the t_{2g}-like ligands are irrelevant altogether and can be discarded from the reference system so that also the parameters $E(t_{2g})$ and $e(t_{2g})$ play no more role. Although slightly different LCAO and Racah parameters were used in this calculation, the results obtained in Ref. 36 are very similar to the ones in the present study; in particular the bands in the valence-band top are essentially identical.

V. RESULTS

The parameters at the stationary point of Ω are listed in Table IV for a temperature of $T=150$ K. Their dependence on temperature turns out to be negligible. Figure 6 shows the temperature dependence of Ω for CoO.

This can be fitted very well by $\Omega(T)=\Omega_0-k_BT\log(12)$. The second term thereby is the entropy due to the degeneracy of the ${}^4T_{1g}$ ground state of d^7 in cubic symmetry. In a

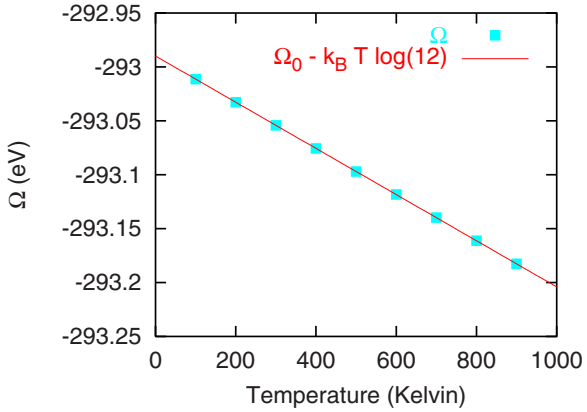

FIG. 6. (Color online) Grand potential $\Omega(T)$ obtained by the VCA for CoO.

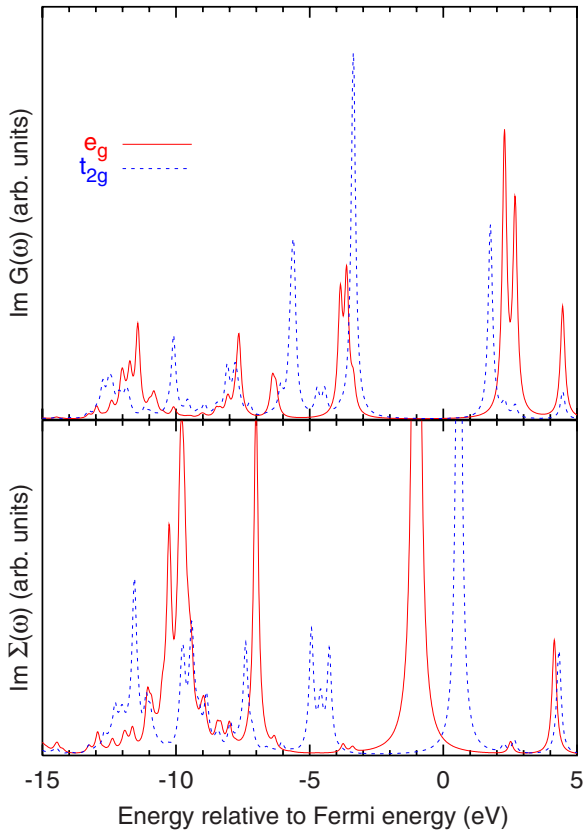

FIG. 7. (Color online) Imaginary part of the Green function (top) and self-energy (bottom) for the reference CoO_6 cluster. The imaginary part of the frequency is −0.1 eV. Parameter values correspond to the stationary point at 150 K.

nonmagnetic system with a wide gap, this is the expected behavior of Ω. This is clearly a trivial result but it should be noted that, for the discussion of a phase transition to a magnetically or orbitally ordered state, the correct description of this entropy is important because this competes with the energy gain due to ordering.

Next we consider the resulting self-energy. Figure 7 shows the spectral density of the CoO_6 cluster and the self-energy at the stationary point for $T=150$ K (all spectra to be shown in the remainder of the paper refer to the stationary points at this temperature; the corresponding parameters of the reference system are listed in Table IV). Due to the cubic symmetry of the cluster, only the diagonal elements of the self-energy are nonvanishing, and these are identical between all e_g and t_{2g} orbitals, respectively. Luttinger has shown[48] that the self-energy has a spectral representation of the form

$$\mathbf{\Sigma}(\omega) = \eta + \sum_{\nu} \frac{\mathbf{S}_{\nu}}{\omega - \zeta_{\nu}}, \tag{20}$$

where the real matrix η is actually the Hartree-Fock potential and the poles ζ_{ν} are all on the real axis. The spectral density of the cluster has a well-defined gap around $\omega=0$ between a charge-transfer peak and the upper Hubbard band. The self-energy for both e_g and t_{2g} electrons has a strong central peak (indicating a pole ζ_{ν} with large residuum S_{ν}) in this gap.

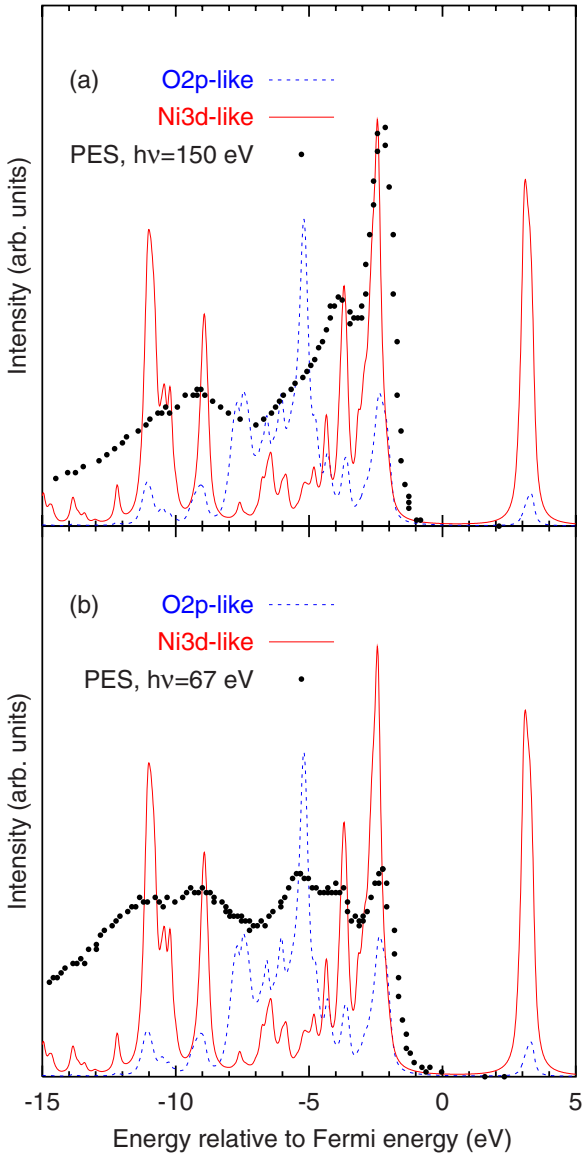

FIG. 8. (Color online) Single particle spectral densities obtained by VCA for NiO (**k** integrated with 110 **k** points in the irreducible wedge of the Brillouin zone) compared to angle-integrated valence-band photoemission data (Ref. 7).

Using the Dyson equation, it is easy to convince oneself that such a strong peak in the self-energy indeed "pushes open" a gap in the pole structure of the Green function. Several other prominent peaks create additional gaps in the spectral density and thus split off the satellite below −9 eV. In addition there are many small peaks near the top of the valence band. Since the poles of the Green function are "sandwiched' between the poles of the self-energy, we thus expect a large number of 3*d*-derived bands with very small dispersion in this energy range.

Next, we proceed to a comparison of $\mathbf{G}(\mathbf{k},\omega)$ to experiment and begin with NiO. Figure 8 compares $\boldsymbol{k}$-integrated spectral densities at $T=150$ K to angle-integrated valence-band photoemission spectra taken by Oh *et al.*[7] at two different photon energies. It is known[49] that, with decreasing photon energy, the intensity of O 2*p*-derived states increases

relative to that of TM3d-derived states—the change of the spectra with photon energy thus allows drawing of conclusions about the character of individual peaks. Moreover, final states with d^{n-1} character are enhanced at a photon energy just above the TM3$p \rightarrow$TM3d absorption threshold so that such energies are particularly suited to identify this type of final state. Accordingly, at $h\nu=150$ eV the experimental spectrum mostly resembles the d-like spectral density whereas at $h\nu=67$ eV, the states at the valence-band top are antiresonantly suppressed. Hence O 2p-derived features become more clearly visible and the satellite at −10 eV is resonantly enhanced. Figures 9 and 10 compare the **k**-resolved spectral function for momenta along (100) ($\Gamma \rightarrow X$) and (110) ($\Gamma \rightarrow K$) to the experimental band dispersion by Shen *et al.*[10]

The spectral density has gap of approximately 4 eV around the chemical potential. This is consistent with experiment[3] but has of course been achieved by the choice of A and Δ. At the top of the photoemission spectrum, $E<0$, there is a high-intensity band complex at binding energies between ≈−3.5 and ≈−2 eV, which was shown to consist of several subpeaks by Shen *et al.*[10] These authors did not actually resolve the dispersion of the individual subpeaks although the data seem to indicate a weak overall "upward" dispersion as one moves $\Gamma \rightarrow X$, which would be consistent with theory. Proceeding to more negative binding energy, the experimental band structure shows a gap of ≈1 eV, and then a group of dispersionless bands between −6 and −4 eV. This is bounded from below by a weakly dispersive band that resembles one of the O 2p-derived bands. In the angle-integrated spectrum [Fig. 8(a)], the topmost of these dispersionless bands produces the "shoulder" at −4 eV. The gap between the topmost band complex and the group of dispersionless bands in the theoretical spectra is not as wide as in experiment but there are clearly several dispersionless bands in approximately the right energy range. The agreement would be very good if the peaks at ≈−3.5 eV in Figs. 9 and 10 were shifted by ≈0.5 eV to more negative binding energy. In addition, the O 2p-derived band can be seen clearly. As can be seen from the band structure in Fig. 1 this band actually has a saddle point at X—this gives rise to a van Hove singularity in the angle-integrated spectrum, which matches very well the peak at ≈−5.5 eV in Fig. 8(b). The sole strongly dispersive feature in the spectrum, namely an O 2p-derived band at binding energies between −6 eV→−9 eV, is again well reproduced by theory. Finally the satellite at binding energies −8 eV→−12 eV consists of at least two subpeaks, as can be seen in Fig. 8(b) and also in the ARPES data.

Next we consider CoO. Figure 11 compares the angle-integrated spectra at different photon energies and the **k**-integrated spectral function obtained by the VCA. Figure 12 shows the dispersion along $\Gamma \rightarrow X$ and ARPES data from Shen *et al.*[5] and Brookes *et al.*[50] The XPS spectrum for CoO starts out with a prominent peak at −3 eV followed by three "humps" at −5, −8, and −12 eV. The VCA gives peaks of d-like spectral weight at roughly these energies although the peak at −5 eV is at slightly too negative energy. The PES spectrum at 40 eV shows additional peaks at −6.5 and −9 eV, which were interpreted as O 2p derived by Shen *et al.*[5] These peaks are also reproduced by the VCA. A little more problematic is the angle-resolved spectrum. Along (100) the VCA predicts a split peak at the top of the valence band at −4 eV. This splitting is not seen in experiment; on the other hand, the spectra were taken at low photon energy

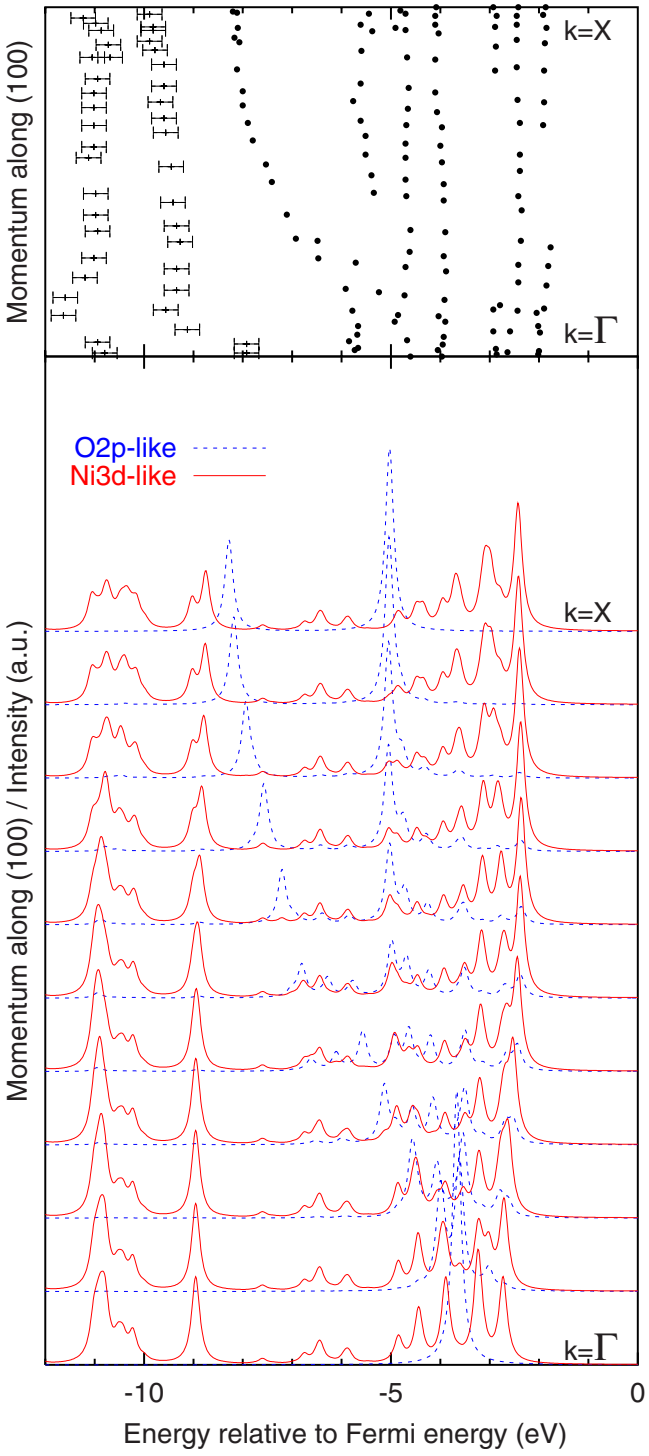

FIG. 9. (Color online) Top: Dispersion of experimental bands measured by ARPES (Ref. 10) in NiO. Bands in the satellite region are given with error bars due to their strong broadening. Bottom: **k**-dependent spectral function for momenta along $\Gamma-X$ in NiO. Lorentzian broadening of 0.05 eV and d-like weight is multiplied by a factor of two.

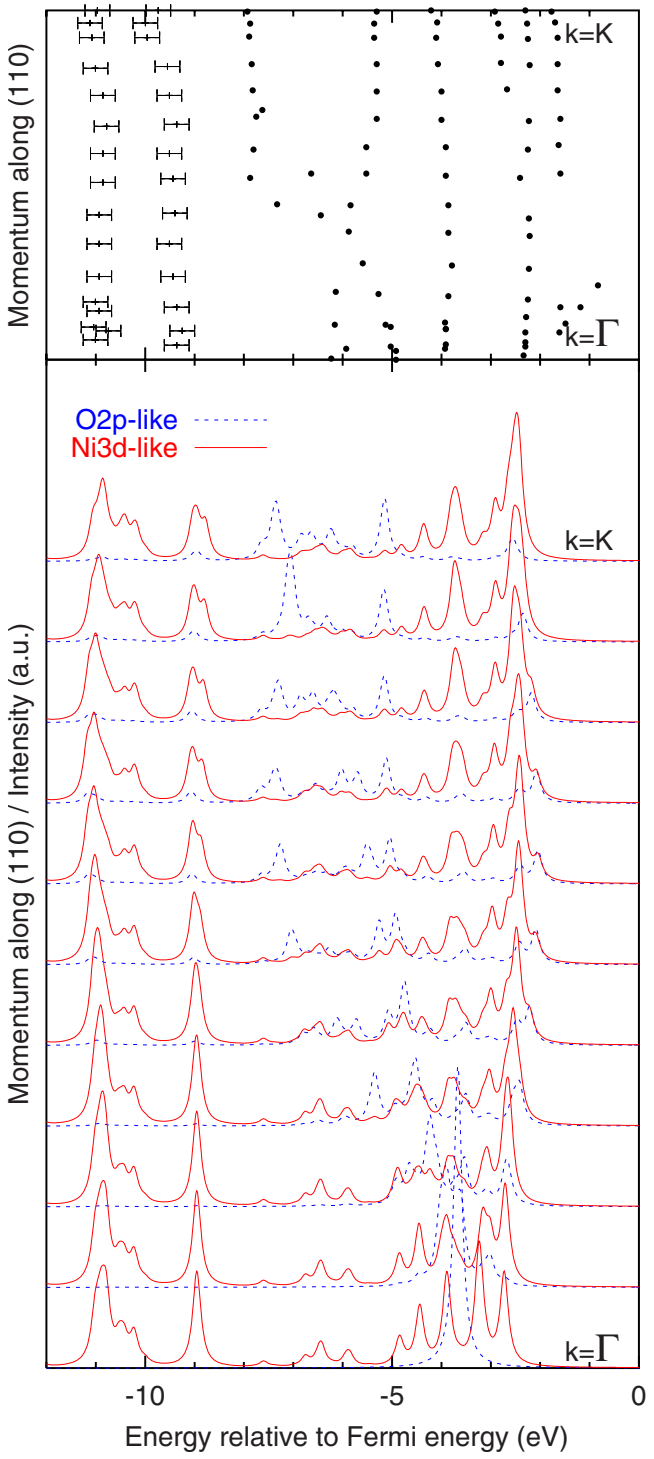

FIG. 10. (Color online) Same as Fig. 9 but for momenta along the (110) direction ($\Gamma - K$).

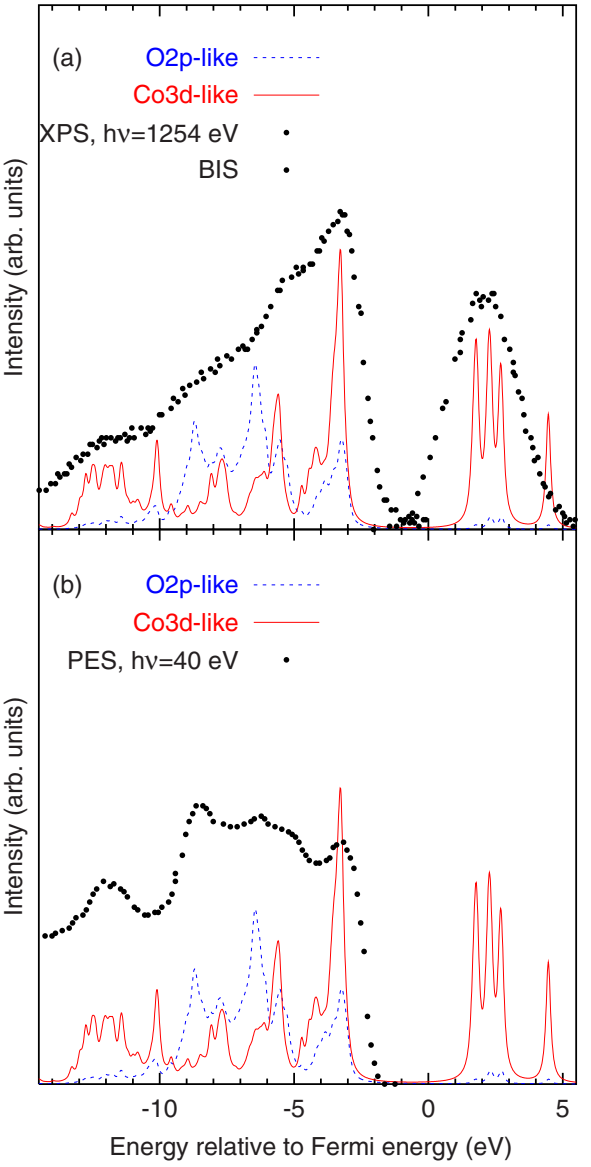

FIG. 11. (Color online) **k**-integrated single particle spectral densities obtained by VCA for CoO compared to valence-band photoemission data. Experimental data in (a) are from Ref. 26 and in (b) from Ref. 5.

where the Co 3*d* states have relatively small weight. There is another *d*-derived band at −6 eV, which corresponds to the second hump in the angle-integrated spectrum. This is crossed by and mixes with one of the O 2*p*-derived bands, which start at Γ at an energy of −5 eV. The presence of these two crossing bands may explain the "wiggly" nature of the bands observed experimentally in this energy range. The presence of more than one band and a possible crossing between these is clearly seen in the data of Shen *et al.* Finally there is the strongly dispersive O 2*p*-derived band at energies of around −8 eV. Surprisingly the experimental dispersions for this band differ somewhat; this may be due to the crossing of this band with the dispersionless Co 3*d*-derived band at −7.5 eV, which leads to a hybridization gap in the O 2*p*-derived band.

Finally we consider MnO. Figure 13 shows the angle-integrated photoemission spectra compared to the result from the VCA. At high photon energy the experimental spectrum matches well the *d*-derived density of states. The single-particle gap and the structure of the valence-band spectrum are reproduced well. It is interesting to note that, although both the Racah parameter *A* and the value U_{CDF} from constrained density-functional theory are considerably smaller for MnO than for NiO (see Table III), the insulating gap is

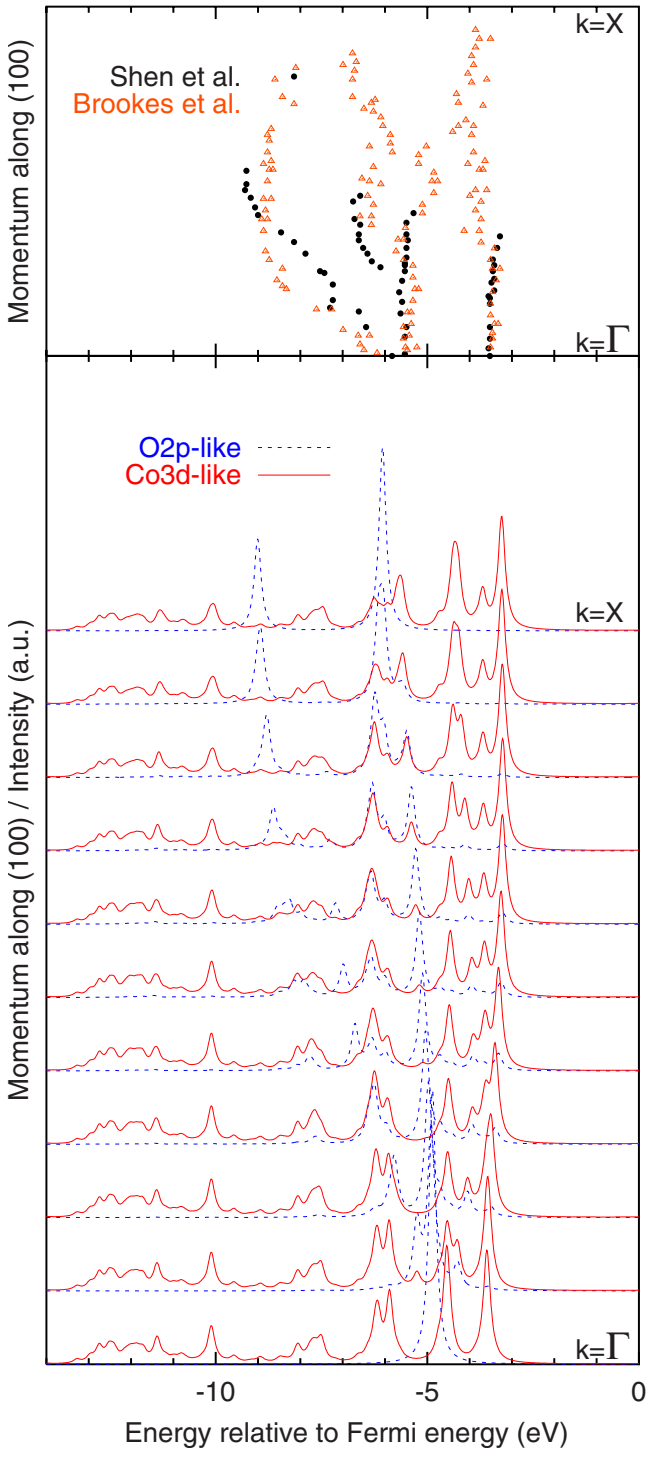

FIG. 12. (Color online) Top: Experimental band structure along (100) as seen in ARPES by Shen *et al.* (Ref. 5) and by Brookes *et al.* (Ref. 50) in CoO. Bottom: **k**-dependent spectral function for momenta along $\Gamma-X$ for CoO. Lorentzian broadening of 0.05 eV and *d*-like weight is multiplied by a factor of two.

actually considerably larger for MnO than for NiO (cf. Fig. 8). This is a consequence of the extra exchange stabilization of the d^5 high-spin state (see Table II), which is automatically accounted for in the VCA calculation.

At a photon energy of 20 eV, the intense peak at −5.5 eV almost disappears and another large peak at −6.5 eV appears, which accordingly must have O 2*p* character. In the theoretical spectra this is reproduced well; the peak at −6.5 eV again is due to a van Hove singularity at *X*. Figure 14 shows the **k**-resolved spectrum along (100). Lad and Henrich[8] performed ARPES measurements on MnO but did not perform any band mapping due to the broad nature of peaks so an experimental dispersion unfortunately is not available.

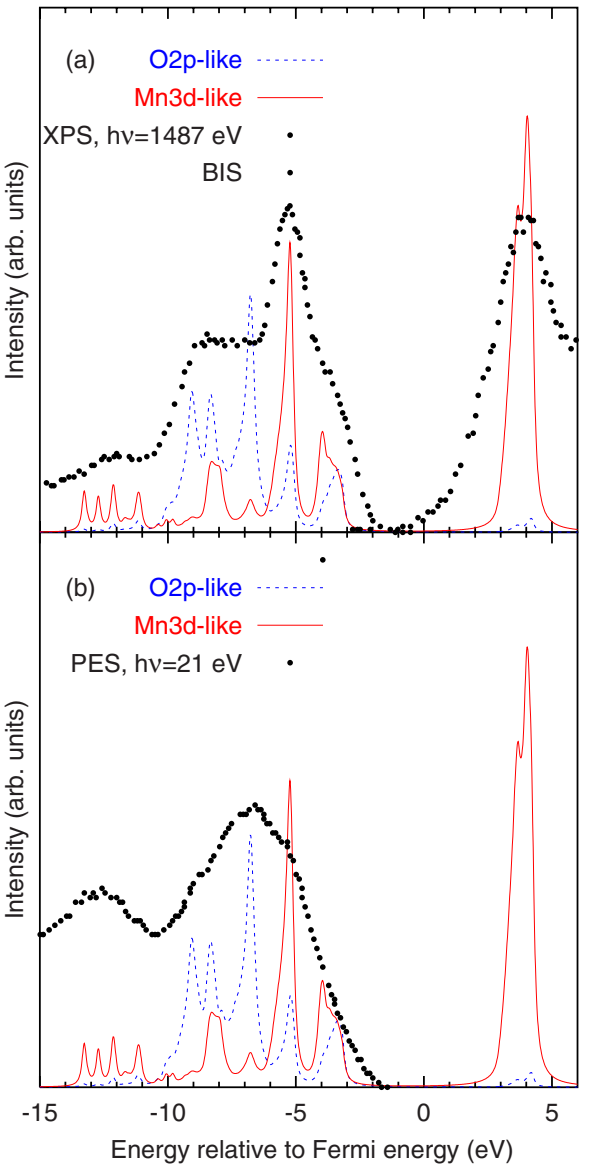

FIG. 13. (Color online) Single particle spectral densities obtained by VCA for MnO compared to valence-band photoemission data. Experimental data in (a) from Ref. 27 and in (b) from Ref. 24.

Lastly we discuss the fine structure of the TM3*d*-derived bands. This is shown in Fig. 15. The band structures of all three compounds have a similar structure: at the top of the band structure, there is a group of dispersive bands that shows a rough similarity with the upper group of bands in the LDA band structure (see Fig. 1), which have mainly TM3*d* character. The total width of this band complex is reduced by a factor of ≈0.5, as compared to LDA. These bands have high spectral weight and produce the intense

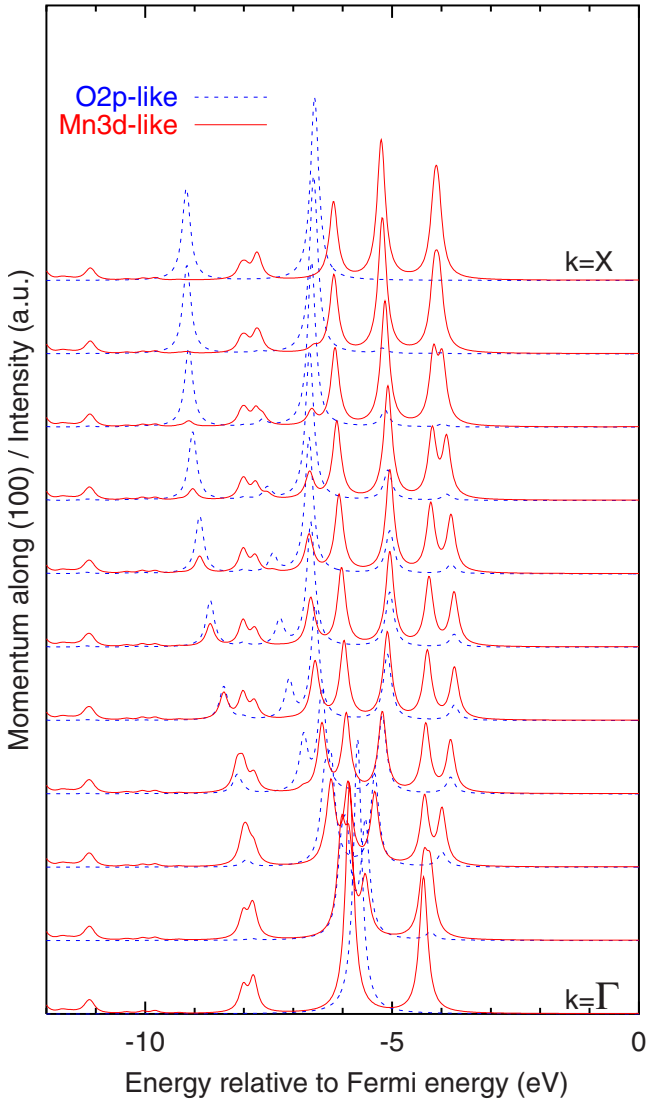

FIG. 14. (Color online) Spectral function for momenta along $\Gamma - X$ in MnO. Lorentzian broadening of 0.05 eV and d-like weight is multiplied by a factor of two. There are no ARPES results available.

peaks at the top of the angle-integrated spectra for NiO and CoO. Separated from this group of dispersive bands, there is then a region with many almost dispersionless bands with relatively low spectral weight. This overall structure can be understood by considering the spectral representation of the self-energy [Eq. (20)] and the equation for the poles of the Green function,

$$\omega + \mu - \epsilon_{\mathbf{k}} - \mathrm{Re}\,\Sigma(\omega) = 0,$$

where we have considered the single-band case for simplicity. Since $\mathrm{Re}\,\Sigma(\omega)$ takes any value between ∞ and $-\infty$ in between two successive poles ζ_ν and $\zeta_{\nu+1}$, there is one band in between any two successive poles of the self-energy. This implies that the distance between these two successive poles is an upper bound for the width of this band, which may be viewed as a kind of correlation narrowing. Moreover, if a pole ζ_ν has only a small residuum, the resulting pole of the

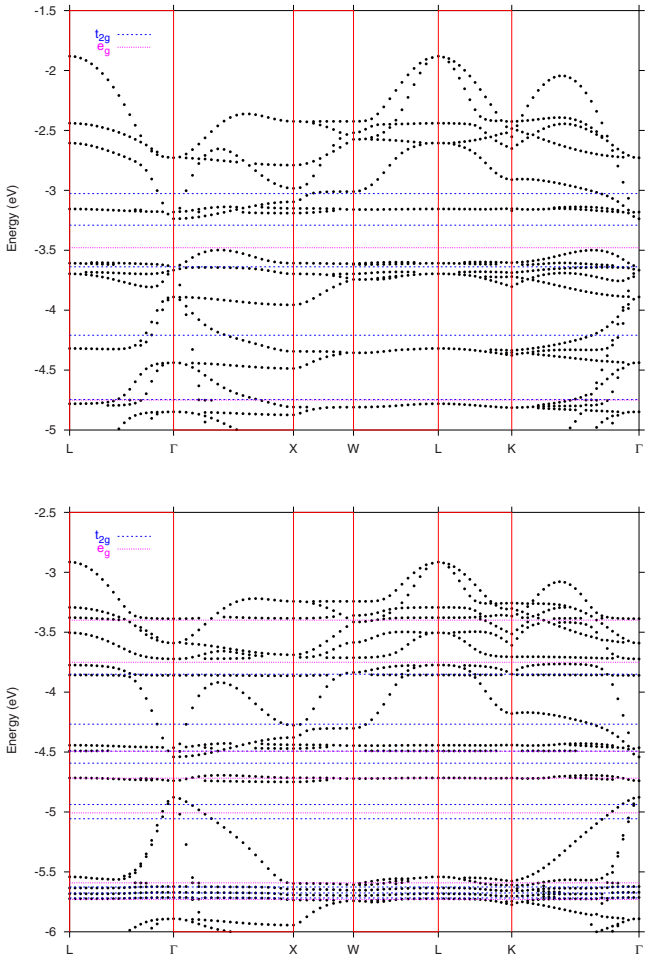

FIG. 15. (Color online) Dispersion of the "subpeaks" in the photoemission spectra of NiO (top) and CoO (bottom). Also shown are the energies of the poles of the self-energy.

Green function will be almost "pinned" very close to it, as can be seen repeatedly in Fig. 15. The topmost group of relatively strongly dispersive bands then is actually above the topmost pole of $\Sigma(\omega)$ in the valence-band region and the dominant "gap opening peak" in the center of the insulating gap (see Fig. 7). Since the separation in energy between these peaks is large—of the order of the insulating gap—these bands still have an appreciable width. The similarity with the LDA band structure is due to the fact that the dispersion of these bands is largely due to direct d-d hopping, which remains operative also when the self-energy is included. While the fine structure of the valence-band top is not really resolved experimentally as yet, at least experiment puts a quite low upper limit—$\leq$0.5 eV along (100)—on the width of the individual bands. The VCA would be consistent with that.

The large number of dispersionless bands at more negative binding energy is produced by the large number of densely spaced poles of the self-energy. These are in turn the consequence of the large number of CEF-split multiplet states in the TMO_6 cluster. Interestingly, at least in the case of NiO where detailed band mapping is available from ARPES, the experimental band structure is quite consistent with this overall structure, namely a group of dispersive

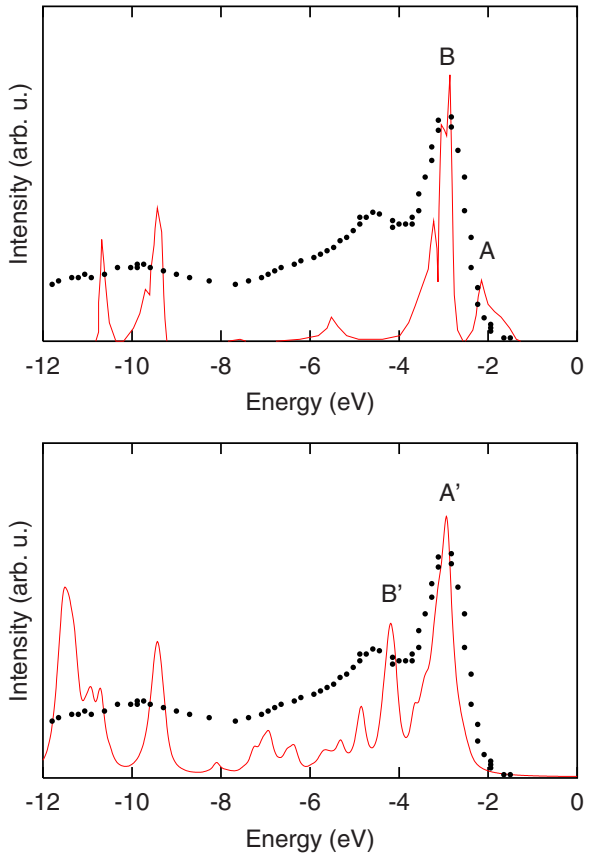

FIG. 16. (Color online) **k**-integrated *d*-like spectral weight obtained by DMFT (top) from Ref. 22 and by VCA (bottom) compared to XPS data from NiO.

bands at the top of the valence band and essentially dispersionless bands at more negative binding energy. The distance between the dispersive band complex and the dispersionless bands is underestimated somewhat by VCA.

To conclude we compare the results of the VCA for NiO with recent LDA+DMFT calculations.[21,22] Figure 16 compares the **k**-integrated spectra and Fig. 17 shows the dispersion along (100). The DMFT results are taken from Yin *et al.*,[22] which have obtained essentially identical results as Kunes *et al.*[21] While the **k**-integrated spectra look similar at first sight, comparison with the band structure shows that there are major differences. In the DMFT spectrum the top of the valence band is formed by a split off peak *A* with low spectral weight. This corresponds to the two topmost bands labeled *A* in Fig. 17. This form of the density of states is actually reminiscent of the results of the three-body-scattering theory of Manghi *et al.*[15] In the VCA spectrum the top of the valence band is formed by an intense peak A', which corresponds to the topmost band complex A' in Fig. 17. The intense peak *B* in the DMFT spectrum on the other hand originates from the band *B* in Fig. 17. The DMFT bands moreover show a rather obvious correspondence with the LDA band structure, resulting in bands with quite strong dispersion. As already noted the VCA differs strongly from LDA and shows a larger number of bands with several of them being practically dispersionless, i.e., corresponding to localized electrons.

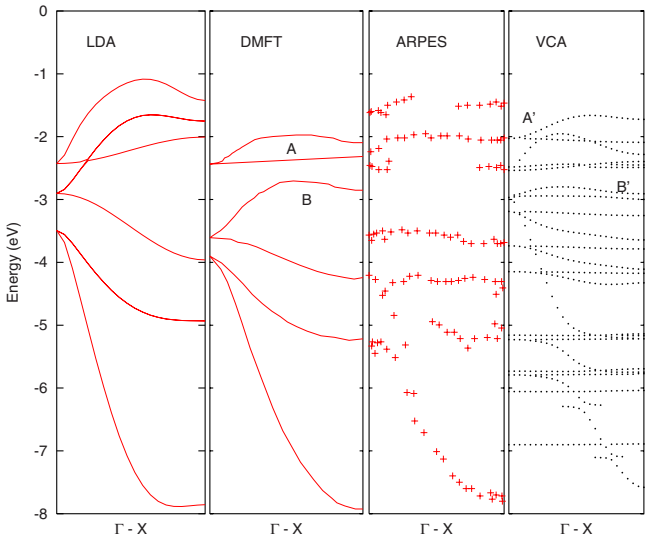

FIG. 17. (Color online) Band structure for NiO along (100) as obtained from LDA, DMFT, ARPES, and VCA. It should be noted that some of the nondispersive bands for VCA have very small spectral weight (see Fig. 9).

Comparing with experiment, the raw data of Shen *et al.*[10] show no indication for the split off bands *A* with low spectral weight as predicted by DMFT. With the exception of the O 2*p*-derived bands, ARPES moreover shows no indication of the wide bands predicted by DMFT; rather there is a number of dispersionless bands as expected on the basis of the VCA. One may say that there are major differences between DMFT and VCA so that further experiments might resolve this discrepancy.

VI. CONCLUSION

To summarize, the variational cluster approximation due to Potthoff allows combination of the powerful cluster configuration-interaction method for transition-metal compounds, due to Fujimori and Minami, with the field-theoretical work of Luttinger and Ward implementing a variational scheme for the electronic self-energy, and constructing an efficient band-structure method for strongly correlated electron compounds. As demonstrated above, a realistic band structure and the full atomic multiplet interaction can be incorporated into the Hamiltonian without problems. The system can be studied at arbitrarily low temperatures and the Green function can be obtained with arbitrary energy resolution. The key numerical problem of finding the stationary point of the grand potential thereby can be solved efficiently by a simple crossover procedure. It has been shown that, in the course of varying the self-energy, there may exist redundant degrees of freedom that leave the grand potential almost unchanged. Such redundant degrees of freedom can be eliminated by simply reducing the number of parameters in the reference system.

The results are quite encouraging in that there is good agreement between the calculated Green function and electron spectroscopies, at least to the extent that ARPES data are available. The good agreement also suggests that the

band structure of NiO, CoO, and MnO is "Coulomb generated" in that the atomic multiplet structure survives with minor modifications. All in all the VCA appears to be a promising tool for the study of realistic models of correlated electron systems. The possibility to treat the multiplet and CEF splitting of the various TM3*d* configurations more or less exactly should make it possible to address magnetic or orbital ordering phenomena in transition-metal compounds.

ACKNOWLEDGMENT

The author would like to thank M. Potthoff for many instructive discussions.

APPENDIX

We show that $\ln[\det \mathbf{G}(\omega)]$ is analytical off the real axis, where $\mathbf{G}(\omega)$ can be either the exact Green function of the reference system or the approximate Green function from the VCA. It is sufficient to prove that all eigenvalues of $\mathbf{G}(\omega)$ have a nonvanishing imaginary part for ω not on the real axis. This is proved in turn if we show that

$$\langle \mathbf{v}|\mathbf{G}(\omega)|\mathbf{v}\rangle = \sum_{i,j} v_i^* G_{ij}(\omega) v_j$$

has a nonvanishing imaginary part for any normalized $\mathbf{v}$. For the exact Green function, we have, using the Lehman representation,

$$\langle \mathbf{v}|\mathbf{G}(\omega)|\mathbf{v}\rangle = \frac{1}{Z}\sum_{\nu',\nu} \frac{|C_{\nu'\nu}|^2}{\omega - (E_\nu - E_{\nu'})}(e^{-\beta\epsilon_\nu} + e^{-\beta\epsilon_{\nu'}}),$$

where $\epsilon_\nu = E_\nu - \mu N_\nu$ and

$$C_{\nu'\nu} = \langle \nu'|\sum_i v_i c_i|\nu\rangle.$$

It follows that for ω in the upper (lower) half plane, all eigenvalues of $\mathbf{G}(\omega)$ have a negative (positive) imaginary part and accordingly all eigenvalues of $\mathbf{G}^{-1}(\omega)$ have a positive (negative) imaginary part. The imaginary part could only be zero if all $C_{\nu'\nu}$ were zero, which is unlikely to occur. A similar proof has been given previously by Dzyaloshinskii.[51] Luttinger has shown that the self-energy $\mathbf{\Sigma}(\omega)$ has a spectral representation of the form

$$\mathbf{\Sigma}(\omega) = \mathbf{g} + \sum_\nu \frac{\mathbf{S}_\nu}{\omega - \zeta_\nu},$$

with a real $\mathbf{g}$.[48] Since $\mathbf{G}(\omega)$ is Hermitian for real ω, the matrices $\mathbf{S}_\nu$ are Hermitian as well; moreover it is positive definite. Namely if one of the matrices $\mathbf{S}_\nu$ would have a negative eigenvalue λ then $\mathbf{G}^{-1}(\zeta_\nu + i\epsilon)$ had the eigenvalue $\frac{i}{\epsilon}\lambda$ plus terms that stay finite as $\epsilon \to 0$; whereas we have shown that all eigenvalues for ω in the upper half plane have positive imaginary parts. It follows immediately that

$$\langle \mathbf{v}|\omega - \mathbf{\Sigma}(\omega)|\mathbf{v}\rangle$$

has a positive (negative) imaginary part for ω in the upper (lower) half plane, which proves that all eigenvalues of the approximate Green functions that are off the real axis have nonvanishing imaginary parts as well.

[1] W. Kohn and L. J. Sham, Phys. Rev. **140**, A1133 (1965).
[2] K. Terakura, T. Oguchi, A. R. Williams, and J. Kubler, Phys. Rev. B **30**, 4734 (1984).
[3] G. A. Sawatzky and J. W. Allen, Phys. Rev. Lett. **53**, 2339 (1984).
[4] O. Tjernberg, S. Söderholm, G. Chiaia, R. Girard, U. O. Karlsson, H. Nylén, and I. Lindau, Phys. Rev. B **54**, 10245 (1996).
[5] Z.-X. Shen, J. W. Allen, P. A. P. Lindberg, D. S. Dessau, B. O. Wells, A. Borg, W. Ellis, J. S. Kang, S. J. Oh, I. Lindau, and W. E. Spicer, Phys. Rev. B **42**, 1817 (1990).
[6] A. Fujimori, K. Terakura, M. Taniguchi, S. Ogawa, S. Suga, M. Matoba, and S. Anzai, Phys. Rev. B **37**, 3109 (1988).
[7] S.-J. Oh, J. W. Allen, I. Lindau, and J. C. Mikkelsen, Jr., Phys. Rev. B **26**, 4845 (1982).
[8] R. J. Lad and V. E. Henrich, Phys. Rev. B **38**, 10860 (1988).
[9] L. C. Davis, Phys. Rev. B **25**, 2912 (1982).
[10] Z. X. Shen, R. S. List, D. S. Dessau, B. O. Wells, O. Jepsen, A. J. Arko, R. Barttlet, C. K. Shih, F. Parmigiani, J. C. Huang, and P. A. P. Lindberg, Phys. Rev. B **44**, 3604 (1991).
[11] J. Hubbard, Proc. R. Soc. London, Ser. A **277**, 237 (1964); **281**, 401 (1964).
[12] A. Svane and O. Gunnarsson, Phys. Rev. Lett. **65**, 1148 (1990).
[13] V. I. Anisimov, I. V. Solovyev, M. A. Korotin, M. T. Czyzyk, and G. A. Sawatzky, Phys. Rev. B **48**, 16929 (1993).
[14] J. Bala, A. M. Oles, and J. Zaanen, Phys. Rev. Lett. **72**, 2600 (1994).
[15] F. Manghi, C. Calandra, and S. Ossicini, Phys. Rev. Lett. **73**, 3129 (1994).
[16] F. Aryasetiawan and O. Gunnarsson, Phys. Rev. Lett. **74**, 3221 (1995).
[17] M. Takahashi and J. I. Igarashi, Phys. Rev. B **54**, 13566 (1996); Ann. Phys. (N.Y.) **5**, 247 (1996).
[18] S. Massidda, A. Continenza, M. Posternak, and A. Baldereschi, Phys. Rev. B **55**, 13494 (1997).
[19] R. Eder, A. Dorneich, and H. Winter, Phys. Rev. B **71**, 045105 (2005).
[20] J. Kunes, V. I. Anisimov, A. V. Lukoyanov, and D. Vollhardt, Phys. Rev. B **75**, 165115 (2007).
[21] J. Kunes, V. I. Anisimov, S. L. Skornyakov, A. V. Lukoyanov, and D. Vollhardt, Phys. Rev. Lett. **99**, 156404 (2007).
[22] Q. Yin, A. Gordienko, X. Wan, and S. Y. Savrasov, Phys. Rev. Lett. **100**, 066406 (2008).
[23] A. Fujimori and F. Minami, Phys. Rev. B **30**, 957 (1984).
[24] A. Fujimori, N. Kimizuka, T. Akahane, T. Chiba, S. Kimura, F. Minami, K. Siratori, M. Taniguchi, S. Ogawa, and S. Suga, Phys. Rev. B **42**, 7580 (1990).
[25] J. van Elp, H. Eskes, P. Kuiper, and G. A. Sawatzky, Phys. Rev. B **45**, 1612 (1992).

[26] J. van Elp, J. L. Wieland, H. Eskes, P. Kuiper, G. A. Sawatzky, F. M. F. de Groot, and T. S. Turner, Phys. Rev. B **44**, 6090 (1991).
[27] J. van Elp, R. H. Potze, H. Eskes, R. Berger, and G. A. Sawatzky, Phys. Rev. B **44**, 1530 (1991).
[28] J. C. Slater, *Quantum Theory of Atomic Structure* (McGraw-Hill, New York, 1960).
[29] J. S. Griffith, *The Theory of Transition-Metal Ions* (Cambridge University Press, Cambridge, England, 1964).
[30] R. Eder, O. Rogojanu, and G. A. Sawatzky, Phys. Rev. B **58**, 7599 (1998).
[31] D. Senechal, D. Perez, and M. Pioro-Ladriere, Phys. Rev. Lett. **84**, 522 (2000).
[32] T. Maier, M. Jarrell, T. Pruschke, and M. H. Hettler, Rev. Mod. Phys. **77**, 1027 (2005).
[33] M. Potthoff, Eur. Phys. J. B **36**, 335 (2003); **32**, 429 (2003).
[34] J. M. Luttinger and J. C. Ward, Phys. Rev. **118**, 1417 (1960).
[35] C. Dahnken, M. Aichhorn, W. Hanke, E. Arrigoni, and M. Potthoff, Phys. Rev. B **70**, 245110 (2004); M. Aichhorn, E. Arrigoni, M. Potthoff, and W. Hanke, *ibid.* **74**, 024508 (2006).
[36] R. Eder, Phys. Rev. B **76**, 241103(R) (2007).
[37] W. Metzner and D. Vollhardt, Phys. Rev. Lett. **62**, 324 (1989); A. Georges, G. Kotliar, W. Krauth, and M. J. Rozenberg, Rev. Mod. Phys. **68**, 13 (1996); G. Kotliar, S. Y. Savrasov, K. Haule, V. S. Oudovenko, O. Parcollet, and C. A. Marianetti, *ibid.* **78**, 865 (2006).
[38] J. C. Slater and G. F. Koster, Phys. Rev. **94**, 1498 (1954).
[39] L. F. Mattheiss, Phys. Rev. B **5**, 290 (1972).
[40] The explicit expressions for the Coulomb matrix elements are given in Eqs. (13-18)–(13-25) of Ref. 28 whereby according to Ref. 29 $F^0=A+7C/5$, $F^2=49B+7C$, and $F^4=63C/5$.
[41] V. I. Anisimov, J. Zaanen, and O. K. Andersen, Phys. Rev. B **44**, 943 (1991).
[42] M. R. Norman and A. J. Freeman, Phys. Rev. B **33**, R8896 (1986).
[43] J. Zaanen, G. A. Sawatzky, and J. W. Allen, Phys. Rev. Lett. **55**, 418 (1985).
[44] J. M. Luttinger, Phys. Rev. **119**, 1153 (1960).
[45] M. Potthoff, Condens. Matter Phys. **9**, 557 (2006).
[46] Y. Ohta, T. Shimozato, R. Eder, and S. Maekawa, Phys. Rev. Lett. **73**, 324 (1994).
[47] A. H. Nevidomskyy, D. Senechal, and A.-M. S. Tremblay, Phys. Rev. B **77**, 075105 (2008).
[48] J. M. Luttinger, Phys. Rev. **121**, 942 (1961).
[49] D. E. Eastman and J. L. Freeouf, Phys. Rev. Lett. **34**, 395 (1975).
[50] N. B. Brookes, D. S.-L. Law, D. R. Warburton, P. L. Wincott, and G. Thornton, J. Phys.: Condens. Matter **1**, 4267 (1989).
[51] I. Dzyaloshinskii, Phys. Rev. B **68**, 085113 (2003).